# Probing Edge Site Reactivity of Oxidic Cobalt Water Oxidation Catalysts

Andrew M. Ullman,[†] Casey N. Brodsky,[†] Nancy Li, Shao-Liang Zheng, and Daniel G. Nocera*

Department of Chemistry and Chemical Biology, Harvard University, 12 Oxford Street, Cambridge, Massachusetts 02138, United States

S *Supporting Information*

ABSTRACT: Differential electrochemical mass spectrometry (DEMS) analysis of the oxygen isotopologues produced by ^{18}O-labeled Co-OEC in $H_2^{16}O$ reveals that water splitting catalysis proceeds by a mechanism that involves direct coupling between oxygens bound to dicobalt edge sites of Co-OEC. The edge site chemistry of Co-OEC has been probed by using a dinuclear cobalt complex. ^{17}O NMR spectroscopy shows that ligand exchange of OH/OH_2 at Co(III) edge sites is slow, which is also confirmed by DEMS experiments of Co-OEC. In borate (B_i) and phosphate (P_i) buffers, anions must be displaced to allow water to access the edge sites for an O−O bond coupling to occur. Anion exchange in P_i is slow, taking days to equilibrate at room temperature. Conversely, anion exchange in B_i is rapid (k_{assoc} = 13.1 ± 0.4 M^{-1} s^{-1} at 25 °C), enabled by facile changes in boron coordination. These results are consistent with the OER activity of Co-OEC in B_i and P_i. The P_i binding kinetics are too slow to establish a pre-equilibrium sufficiently fast to influence the oxygen evolution reaction (OER), consistent with the zero-order dependence of P_i on the OER current density; in contrast, B_i exchange is sufficiently facile such that B_i has an inhibitory effect on OER. These complementary studies on Co-OEC and the dicobalt edge site mimic allow for a direct connection, at a molecular level, to be made between the mechanisms of heterogeneous and homogeneous OER.
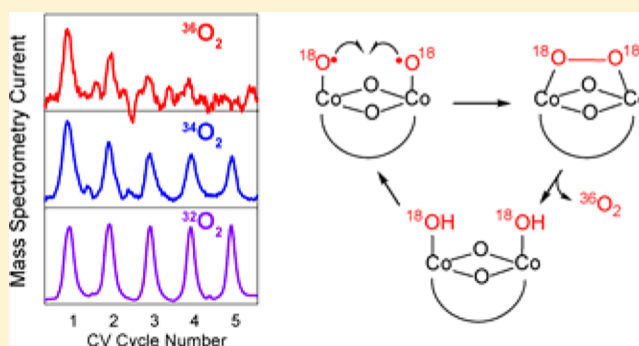
INTRODUCTION

The large scale implementation of renewable energy requires catalysts that can extract electrons and protons from water at low thermodynamic overpotentials.[1,2] The electron and proton reducing equivalents may be used directly as a fuel in the form of hydrogen or combined with CO_2 to furnish liquid fuels. Metal oxides have long been studied for this purpose, though most investigations have focused on the pH extremes, primarily precious metal oxide (e.g., RuO_2) catalysts in acidic solutions,[3,4] and first-row transition-metal oxide catalysts (e.g., cobalt oxides) in alkaline solutions.[5] Although there are advantages to reducing ohmic drops at extreme pH, large scale implementation of an energy conversion system using concentrated acid and base, especially in a distributed fashion, is impractical. Moreover, direct conversion of CO_2 and hydrogen to fuels is best accomplished at neutral pH, where pH gradients may be mitigated under flow conditions.[6] To this end, we have developed cobalt oxygen evolving catalysts (Co-OECs) that are active in neutral or near-neutral pH regimes.[7,8] In these systems, the active sites are cobaltate clusters,[9−12] which are likely to be the active sites in cobalt oxides operating in strong base as well. High-resolution transmission electron microscopy (HRTEM) has shown that crystalline cobalt oxides in neutral and alkaline solutions form amorphous overlayers comprising cobaltate aggregates,[13−16] which are the likely active

sites for catalysis as opposed to the native oxide. This has led to the proposal that the catalysis of Co-OECs and cobalt oxides in neutral and concentrated base occurs at edge sites of the cobaltate clusters, with a dicobalt active site as the minimal structural unit that supports catalysis (Scheme 1).[17−19]

Scheme 1. Dicobalt Edge Site Is the Dimensionally Reduced Active Site of Co_3O_4 and Co-OEC
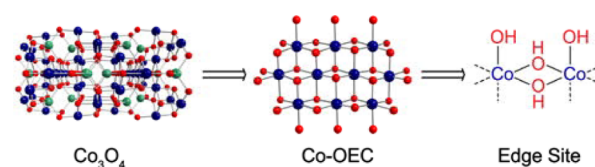
Nevertheless, little is known experimentally about the oxygen evolution reaction (OER) at edge sites of cobaltate clusters. Time-resolved infrared spectroscopy of Co_3O_4 nanoparticles in pH = 8 solution suggests the presence of superoxide/oxo intermediates formed at dicobalt edge sites during OER catalysis.[18] In a separate study, sensitive mass spectrometric measurements show the incorporation of a solvent $H_2^{18}O$ label

into evolved dioxygen following water oxidation catalyzed by Co/methylenediphosphonate (Co/M2P) oxide nanoparticles.[20] Initial turnover analysis of the O_2 isotopologue ratio following the rapid (and simultaneous) injection of $H_2^{18}O$ and $Ru(bpy)_3^{3+}$ led to a proposed mechanism for water oxidation involving edge-site-mediated O−O bond formation via direct intramolecular coupling. Consistent with Scheme 1, the data from these experiments also suggested ∼2 cobalt atoms per catalytic site.

We report here mechanistic studies of Co-OECs and complementary investigations of molecular dicobalt analogs to shed light on the mechanism of OER at edge sites of cobaltic oxides. We have investigated the isotopologue distribution of labeled O_2 evolved from Co-OEC-mediated OER using differential electrochemical mass spectrometry (DEMS). This technique[21−23] identifies the distribution of ^{18}O in evolved dioxygen from an ^{18}O-labeled Co-OEC catalyst (in $H_2^{16}O$) under the exact electrochemically driven conditions of OER as a function of applied potential[24,25] and in doing so offers insights into the OER mechanism. To this end, the DEMS data support the notion that turnover is occurring at the edge sites of Co-OEC and that O−O bond formation occurs, at least in part, by intramolecular coupling between oxygen atoms ligated to cobalt at the edge sites. To further address the chemistry of edge sites, we prepared a dicobalt complex wherein a diamond $Co_2(OH)_4$ core (Scheme 2) is stabilized by the six coordinate

Scheme 2. Synthesis of Edge Site Mimic $[1(OH_2)_2]^{4+}$ Using the Ligand DPEN
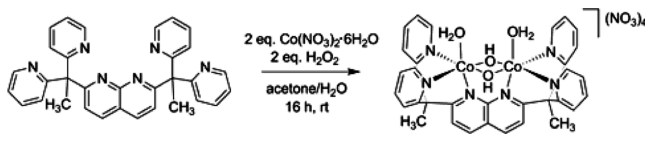
ligand dipyridylethane naphthyridine (DPEN). The complex is akin to the first-row metal complexes of DPEN (and its fluorinated analog, DPFN) prepared by Tilley and co-workers.[26−28] We have identified edge site equilibrium reactions that deliver the open coordination sites needed for the intramolecular coupling reaction identified by the DEMS experiment. The kinetics of phosphate (P_i) and borate (B_i) binding to dicobalt centers differ by many orders of magnitude due to facile coordination chemistry between boric acid, $B(OH)_3$, and the edge of the cobalt dimer. Consistent with this observation, an inverse dependence of the activity of Co-OECs on $[B_i]$ establishes the necessity of a *syn* configuration of the terminal hydroxo moieties of the diamond $Co_2(OH)_4$ core edge site. Together, the results of the authentic Co-OEC and dicobalt model compound demonstrate the important role of edge sites in controlling the OER activity of cobalt-oxide catalysts.

■ RESULTS

Differential Electrochemical Mass Spectrometry of Co-OEC. DEMS was used in conjunction with isotope labeling to probe the mechanism of O−O bond formation in Co-OEC thin-film catalysts. Catalyst films were deposited from solutions of 1 mM Co^{2+} in 100 mM KP_i at pH 7 in 97% $H_2^{18}O$ by performing a controlled potential electrolysis at 0.9 V vs Ag/AgCl (all potentials are referenced to Ag/AgCl unless noted otherwise) and passing a total charge of 10 mC. This labeled

catalyst film was then inserted into the electrochemical flow cell of the DEMS instrument (instrument details provided in SI), while electrolyte (100 mM KP_i and 200 mM KNO_3 in $H_2^{16}O$ at pH 7) of natural isotopic abundance was flowed through the cell at a rate of 60 mL/h. An electrolyte flow for 30 min was maintained so that mass spectrometric (MS) O_2 baselines equilibrated to constant values. Because we anticipated fast exchange of surface OH/OH_2 species with bulk water at exposed Co(II) centers, the catalyst film was held at a constant potential of 0.9 V during this equilibration period to maintain an oxidation state of Co(III). Five consecutive cycles of cyclic voltammograms (CVs) were performed from 0.9 to 1.1 V at 10 mV/s and the three isotopologues $^{32}O_2$, $^{34}O_2$, and $^{36}O_2$ were detected by the online MS in real time (Figure 1). The CVs
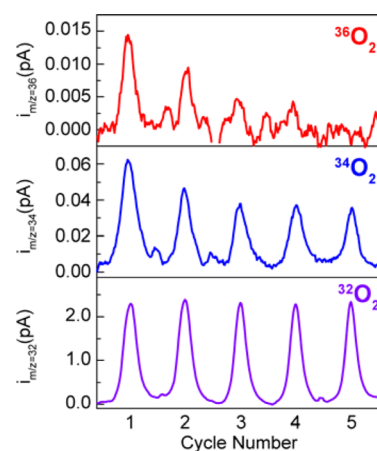

Figure 1. DEMS experimental data for ^{18}O-labeled Co-OEC operated in unlabeled P_i buffer of natural abundance at pH 7. Five consecutive CVs are scanned from 0.9 to 1.1 V vs Ag/AgCl at 10 mV/s, while MS ion current is detected for mass channels m/z = 32, 34, 36 (bottom to top).

plateau at a maximum current of −0.5 mA due to sluggish ion conductance limited by the narrow capillaries of the flow cell, and each cycle plateaus to the same maximum current, indicating no loss of active catalyst during the experiment. All three isotopologues of O_2 were detected in the first four CV cycles; the $^{36}O_2$ signal is weak and by the fifth cycle the signal level could not be distinguished from the noise in the baseline.

Interpreting the data in Figure 1 requires knowledge of the exchange rate of OH/OH_2 bound to the Co(III) centers with bulk water on the time scale of the DEMS experiment. To examine the issue of exchange, the experiment in Figure 1 was repeated but using a longer equilibration time of 5 h, during which the catalyst was held at 0.9 V to maintain an oxidation state of Co(III). The result of this experiment at longer equilibration time (Figure S1) was the same as Figure 1 with a slight decrease in overall signal intensity. All three isotopologues were detected in non-negligible amounts in the first four cycles, while $^{36}O_2$ signal falls to the level of noise by the fifth cycle.

Whereas Co(III) is stable to OH/OH_2 exchange over hours of the DEMS experiment, Co(II) is not. The Co-OEC thin-film catalyst was equilibrated for a 30 min period with no applied potential bias. The films were then scanned from 0.6 to 1.1 V at a rate of 1 mV/s (Figure S2). Under these conditions, a significant population of Co(II) centers is generated in the film before the onset of OER catalysis. For this DEMS experiment,

only $^{32}O_2$ is detected to any significant extent (Figure S2); $^{34}O_2$ was detected at low signal intensity only on the first two scans, and no $^{36}O_2$ was detected above the level of noise. These results informed us that a reliable DEMS experiment required that Co-OEC films be maintained in the Co(III) oxidation state (i.e., at 0.9 V applied potential), as performed for Figure 1.

Molecular Co$_2$(III,III) Edge Site Model. To acquire a more precise knowledge of OH/OH$_2$ exchange at Co(III) edge sites, a dicobalt edge-site model of Co-OEC, $[1(OH_2)_2]^{4+}$, was employed. The complex (Scheme 2) features a dicobalt Co$_2$(III,III) (OH)$_2$ diamond core with *syn* geometry of terminal aquo/hydroxo ligands. This core is supported by a dipyridyl-ethane naphthyridine (DPEN) ligand, which had previously been reported by Tilley et al. for stabilizing dinuclear copper complexes[28] and first-row metals (using the fluorinated analog, DPFN).[26,27] $[1(OH_2)_2]^{4+}$ was assembled by oxidation of a mixture of 2:1 Co(NO$_3$)$_2$:DPEN with 2 equiv of aqueous peroxide (Scheme 2). Following precipitation with acetone, elementally pure compound was isolated as a pink solid. Single crystals of the complex were isolated from a pH = 5.5 aqueous solution in the presence of PF$_6$ anions. The solid-state structure of these crystals is shown in Figure 2 and showcases a dimer of
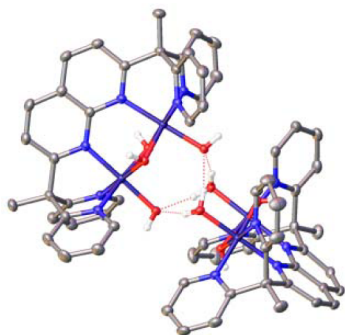

Figure 2. Solid-state structure of the hydrogen-bonded dimer $[1(OH_2)_2|(HO)_21]^{6+}$ with PF$_6$ anions, solvent molecules, and DPEN hydrogen atoms removed for clarity. Atoms are color-coded: gray (C), blue (N), red (O), dark blue (Co), and white (H).

dimers complex, $[1(OH_2)_2|(HO)_21]^{6+}$, which is held together by the hydrogen bonds of an H$_6$O$_4$ dianion. The pK_as of the terminal aqua ligands in $[1(OH_2)_2]^{4+}$ were measured by titration with NaOH and found to be pK_{a1} = 5.08 and pK_{a2} = 6.75 (Figure S3), supporting the notion that the mono-deprotonated species, $[1(OH)(OH_2)]^{3+}$, is stable in the pH regime in which the crystals were grown.

The cyclic voltammogram of $[1(OH_2)_2]^{4+}$ in B$_i$ buffer (pH = 9.2) shows no appreciable current signature beyond background at potentials <1.8 V vs NHE (Figure S4), indicating that oxidation of the complex to a Co(IV) species is not possible within the electrochemical window of this experiment. This electrochemical inertness to higher oxidation states contrasts that of Co-OEC, which exhibits access to Co(IV) at reasonably low potentials (~1.1 V vs NHE). Presumably, the polymetallic cobaltate cluster allows for redox leveling to attain the Co(IV) oxidation state, which is not accessible for the bimetallic core of $[1(OH_2)_2]^{4+}$. Accordingly, $[1(OH_2)_2]^{4+}$ does not support OER.

Water/Hydroxo Exchange at Co$_2$(III,III) Edge Site. The OH/OH$_2$ exchange was measured by ^{17}O NMR spectroscopy. The all-Co(III) complex $[1(OH_2)_2]^{4+}$ was labeled with ^{17}O by heating in 40% H$_2^{17}O$ enriched water at pH 0 at 60 °C for 3 d,

after which it was precipitated out of solution by acetone and collected as a solid. At this temperature and pH, both bridging and terminal OH/OH$_2$ moieties were able to incorporate the ^{17}O label. Labeled compound was freshly dissolved (100 mM) in an unlabeled buffer solution of 50 mM KP$_i$ at pH = 7, and ^{17}O NMR spectra were collected every 20 min for 28 h at room temperature (Figure 3a). Three NMR peaks were observed.
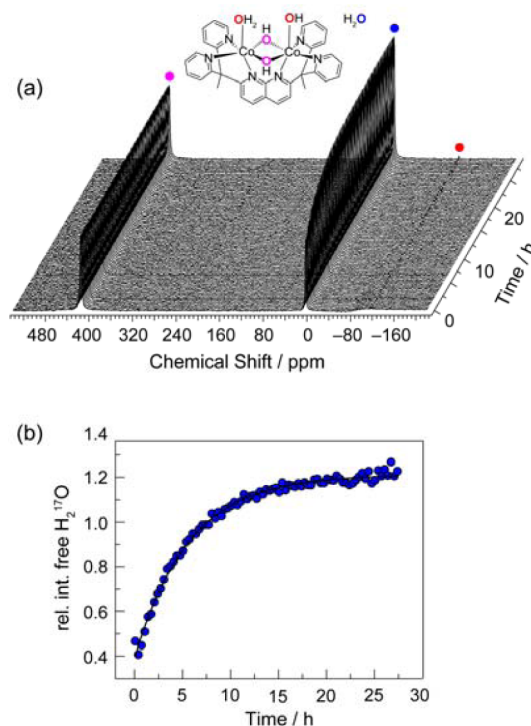

Figure 3. (a) ^{17}O NMR of ^{17}O-labeled $[1(OH)(OH_2)]^{3+}$ in 50 mM natural abundance KP$_i$ buffer at pH 7 over the span of 28 h at room temperature. (b) Relative integration of the free H$_2^{17}O$ peak (int. free H$_2^{17}O$/int. bound bridging ^{17}OH) versus time, fit to a mono-exponential growth curve.

The peak at 420 ppm does not change during the 28 h, corresponding to bridging ^{17}OH. The peak at 0 ppm increases exponentially, corresponding to free H$_2^{17}O$ and the peak at −100 ppm decreases, corresponding to the terminal $^{17}OH/^{17}OH_2$ groups.[29] The broadness of this peak may be attributed to the mixture of terminal OH and OH$_2$ groups combined with fast proton exchange with solvent. The growth of the peak at 0 ppm for free H$_2^{17}O$ is due solely to exchange of the ^{17}O label from the terminal OH/OH$_2$ positions of the complex into bulk water; thus this sharp peak was integrated for quantitative analysis. The integration of the free H$_2^{17}O$ peak relative to the integration of bridging ^{17}OH was plotted against time (Figure 3b) and fit to a monoexponential curve, yielding a rate constant k_{ex} = 4.9 ± 0.1 × 10^{-5} s^{-1}, with a lifetime of 5.7 ± 0.2 h. This result is consistent with the DEMS experiment; namely that exchange of terminal OH/OH$_2$ groups at Co(III) centers is slow, occurring on the order of hours.

Anion Exchange at Co$_2$(III,III) Edge Site. In buffer solutions of borate (B$_i$) and phosphate (P$_i$), edge sites of Co-OEC are available for ligation. These anions must dissociate for OER to be performed. Complex **1** provides an ideal platform to examine the binding of B$_i$ and P$_i$ to a dicobalt edge site. The binding interaction with B$_i$ was followed by using electronic

absorption spectroscopy. The concentration of borate buffer B_i was adjusted by adding different volumes of a KB_i (1 M) stock solution to a $[\mathbf{1}(OH_2)_2][(NO_3)_4] = 250\ \mu M$ solution; the samples were maintained at pH = 8.8, and ionic strength $I = 1$ M was maintained with addition of KNO_3. As shown in Figure 4, the titration of $[\mathbf{1}(OH)_2]^{2+}$ (pH = 8.8) with increasing
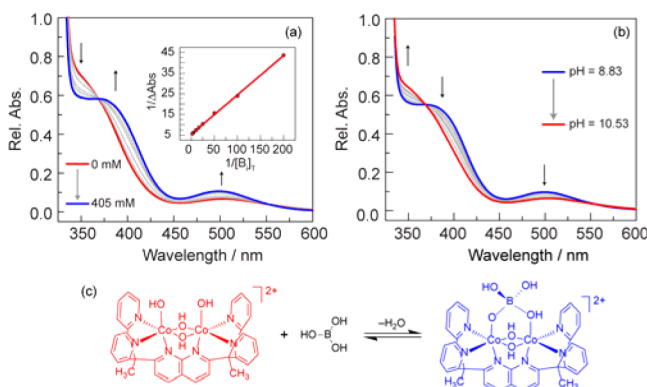

Figure 4. (a) UV−vis absorption changes during titration of 250 μM $[\mathbf{1}(OH)_2]^{2+}$ with borate buffer at pH = 8.8 and $I = 1$ M. (Inset) Benesi−Hildebrand plot with respect to total borate concentration, $[B_i]_T$. (b) UV−vis absorption changes during a pH titration of a solution of 250 μM $[\mathbf{1}(OH)_2]^{2+}$ and 225 mM $[B_i]_T$. (c) Color-coded schematic of the binding event between the $[\mathbf{1}(OH)_2]^{2+}$ and $B(OH)_3$.

concentrations of buffer, $[B_i]_T$, led to the growth of a shoulder at $\lambda = 390$ nm and an increase in intensity of the d−d transition at $\lambda = 499$ nm, with an isosbestic point at $\lambda = 369$ nm. Analysis of the Benesi−Hildebrand plot of this data (Figure 4a inset) furnishes a binding constant with respect to total borate buffer concentration, $[B_i]_T$, of $K_{obs} = 28\ M^{-1}$. The total concentration of boron species $[B_i]_T$ in the buffer is the sum of the concentrations of boric acid, $[B(OH)_3]$, and borate anion, $[B(OH)_4^-]$. When $[B_i]_T$ was held constant at 250 mM, and the pH was increased gradually from 8.8 to 10.5 (Figure 4b), the spectrum reverts to that of the unbound $[\mathbf{1}(OH)_2]^{2+}$. As increasing the pH effectively increases the $B(OH)_4^-$ concentration and reduces the concentration of $B(OH)_3$ in solution, the result of Figure 4b indicates that $B(OH)_4^-$ does not bind to $[\mathbf{1}(OH)_2]^{2+}$, and it is the $B(OH)_3$ component of the buffer that binds to the dicobalt center of $[\mathbf{1}(OH)_2]^{2+}$ (Figure 4c). The association constant for boric acid is given by

$$K_{B(OH)_3} = K_{obs}\left(1 + \frac{K_a}{[H^+]}\right) \tag{1}$$

where $K_a = 10^{-8.6}$ M is the acid dissociation constant of boric acid at $I = 1$ M,[30] and at pH = 8.8, $[H^+] = 10^{-8.8}$ M. Substituting the K_{obs} of 28 M^{-1} that was extracted from the Bensei−Hildebrand analysis furnishes $K_{B(OH)_3} = 73\ M^{-1}$ for the equilibrium binding of $B(OH)_3$ to $[\mathbf{1}(OH)_2]^{2+}$. A Job plot constructed from the titration of $[\mathbf{1}(OH)_2]^{2+}$ with B_i (Figure S5) maximizes at a molar fraction of $B(OH)_3 = \sim0.5$, consistent with a 1:1 association complex depicted in Figure 4c.

The association of $B(OH)_3$ to $[\mathbf{1}(OH)_2]^{2+}$ occurs rapidly upon mixing, and hence stopped flow measurements were required to measure the kinetics of association ($k_{assoc}(B(OH)_3)$) at room temperature. The extent of the reaction was monitored by following the growth (seen in Figure 4a) of the absorption at $\lambda = 390$ nm. Under pseudo-first-order conditions, the data were modeled well with a monoexponential fit, (Figure

5a, all fits, not shown, possess R^2 values exceeding 99.9%). The observed rate constant varied linearly with $[B(OH)_3]$ (Figure
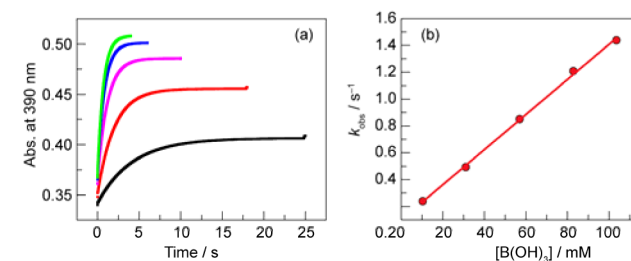

Figure 5. (a) Stopped-flow kinetic plots of the reaction at pH = 8.8 between 500 μM $\mathbf{1}(OH)_2^{2+}$ and $[B_i]_T$ at 250 mM (green), 200 mM (blue), 137.5 mM (magenta), 75 mM (red), and 25 mM (black). (b) Linear relationship between $[B(OH)_3]$ and observed rate constant from which the second-order rate constant is determined.

5b), implying a first-order dependence; this result was consistent with that from the Job plot. The pseudo-first-order rate as a function of $[B(OH)_3]$ yielded a second-order rate constant of $k_{assoc}(B(OH)_3) = 13.1 \pm 0.4\ M^{-1}\ s^{-1}$ at 25 °C. Variable-temperature experiments were also conducted (Figure S6), and an Eyring analysis of the second-order rate constant revealed an activation enthalpy of $\Delta H^{\ddagger} = 34.5 \pm 0.7\ kJ\ mol^{-1}$ and activation entropy of $\Delta S^{\ddagger} = -107 \pm 3\ J\ mol^{-1}\ K^{-1}$.

The UV−vis absorbance spectral changes resulting from anion association to the dicobalt center of $[\mathbf{1}(OH)_2]^{2+}$ in P_i buffer are qualitatively similar to that observed for B_i buffer but evolve over a much longer time scale. As shown in Figure 6, a
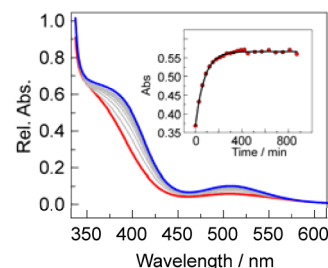

Figure 6. UV−vis absorption changes of a mixture of 250 μM $[\mathbf{1}(OH)_2]^{2+}$ and 167 mM KP_i at pH = 8.5 and 70 °C. (Inset) Monoexponential fit to the change in absorbance at 390 nm versus time.

shoulder near 400 nm appears with an attendant increase in intensity at $\lambda = 507$ nm in the absence of isosbestic points. At an elevated temperature of 70 °C, these absorption features require ~10 h to attain equilibrium (Figure 6a inset); as a comparison, the color changes associated with $B(OH)_3$ binding appear instantaneous to the eye at room temperature. At pH = 8.5, the speciation of P_i buffer is largely HPO_4^{2-}. The spectral changes for the association of HPO_4^{2-} to $[\mathbf{1}(OH)_2]^{2+}$ were monitored under pseudo-first-order conditions. A plot of the observed rate constant as a function of $[P_i]$ from 46 to 167 mM exhibits poor linearity (Figure S7), indicating more complicated kinetics for HPO_4^{2-} association. This contention is also supported by ^1H NMR experiments. Upon mixing 5 mM $[\mathbf{1}(OH)_2]^{2+}$ with 333 mM KP_i ($I = 1$ M) at pH = 8.6, the intensity of the resonances associated with $[\mathbf{1}(OH)_2]^{2+}$ decreases, while peaks (many of which were overlapping) associated with two new species appear (Figure S8).

Monitoring the integrated intensity with time reveals biexponential kinetics for the decrease in $[1(OH)_2]^{2+}$ (Figure S9). The faster component has a lifetime of 4.9 ± 0.8 h, while the slower component exhibits a lifetime of 160 ± 30 h. The structural chemistry of phosphate with compound **1** is consistent with these observations. Both 1:1 and 2:1 phosphate:dicobalt complexes are known. A 2:1 dimer structure $[1(O_2PO_2)1]^{5+}$ is known to be a stable species for the similar metal–ligand DPFN architecture.[28] We report here the 1:1 complex shown in Figure 7. The crystal structure of
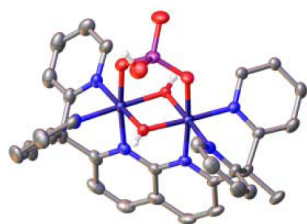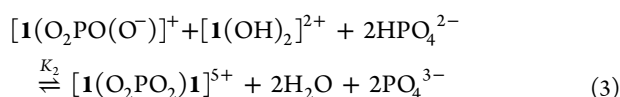

Figure 7. Solid-state crystal structure of phosphate bound complex $[1(O_2PO(OH))]^{2+}$ with ClO_4^- anions, solvent molecules, and DPEN hydrogen atoms removed for clarity. Atoms are color-coded: gray (C), blue (N), red (O), dark blue (Co), white (H), and purple (P).

$[1(O_2PO(OH))]^{2+}$ was obtained from a mixture of $[1(OH_2)_2]^{4+}$ and 10 equiv of P_i that was heated at 90 °C for 3 d at pH = 3. Thus, at pH = 3, the 1:1 complex forms from complexation by $H_2PO_4^-$ to the aquo species $[1(OH_2)_2]^{4+}$. However, at I = 1 M and pH = 8.6 used in the kinetics measurements, $[1(OH)_2]^{2+}$ is the stable species, and 99% of the phosphate buffer is the monoacidic form, HPO_4^{2-}. Therefore, we attribute the short lifetime component of Figure S9 to the facile formation of the 1:1 complex, $[1(O_2PO(OH))]^{2+}$, which we expect to be deprotonated at pH = 8.6:

$$[1(OH)_2]^{2+} + 2HPO_4^{2-}$$
$$\overset{K_1}{\rightleftharpoons} [1(O_2PO(O^-))]^+ + 2H_2O + PO_4^{3-} \qquad (2)$$
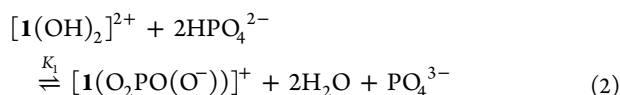
In the subsequent slower reaction (i.e., the longer lifetime component in Figure S9), deprotonated $[1(O_2PO(OH))]^{2+}$ reacts with another $[1(OH)_2]^{2+}$ to give the dimer structure, $[1(O_2PO_2)1]^{5+}$:

$$[1(O_2PO(O^-))]^+ + [1(OH)_2]^{2+} + 2HPO_4^{2-}$$
$$\overset{K_2}{\rightleftharpoons} [1(O_2PO_2)1]^{5+} + 2H_2O + 2PO_4^{3-} \qquad (3)$$

Using this model for P_i binding, a lower limit for the association constants could be estimated from the relative distributions of the bound and unbound complexes after 25 d. The two relevant association constants were estimated to be $K_1 = 0.08$ M^{-1} for formation of 1:1 complex and $K_2 = 0.5$ M^{-1} for the dimer structure (see SI for details).

OER Activity of Co-OEC in B_i. To correlate the insights afforded from these molecular model studies with the interaction of anions at edge sites within Co-OEC films, we examined the dependence of OER activity of Co-OEC with anions. Whereas the activity of Co-OEC has been shown to exhibit a zero-order dependence on $[P_i]$,[12] the dependence of OER activity of CoP_i and CoB_i films in B_i has heretofore not been defined. Co-OEC films were deposited from Co^{2+} solutions containing either B_i buffer (Figure 8a) (CoB_i films) or P_i buffer (Figure 8b) (CoP_i films) onto glassy carbon
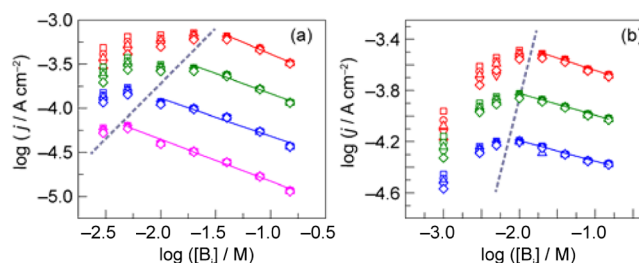

Figure 8. Dependence of the water oxidation current density on $[B_i]$ for 24 mC/cm^2 thick films of (a) CoB_i and (b) CoP_i at pH = 8.6 and I = 1 M using a rotating disk electrode at potentials vs Ag/AgCl of 0.95 V (red), 0.925 V (green), 0.90 V (blue), and 0.875 V (magenta). The shaped data points correspond to rotation rates in rpm of 2500 (square), 1600 (circle), 1225 (up triangle), 900 (down triangle), and 625 (diamond). Slopes of the linear fits (solid lines) are approximately (a) − 0.47 and (b) − 0.18.

rotating disk electrodes. The current density ($\log(j)$) associated with OER was monitored as a function of $[B_i]$, applied potential, and rotation rate. For both films, there exist two regions of interest. In the region of low $[B_i]$ (i.e., left of the dashed lines in Figure 8), the current density increases with increasing $[B_i]$. At a given $[B_i]$, the current density depends on the rotation rate (i.e., spread in current density at a given $[B_i]$ for a given potential); with increasing $[B_i]$ the spread in current density at a given $[B_i]$ converges with rotation rate. As we have shown, both the dependence on rotation rate (at a given $[B_i]$) and the increase in $\log(j)$ with $[B_i]$ (at a given potential) are indicative of partial mass transport control of protons diffusing from the catalyst films, mediated by the diffusion of buffer from solution into the catalyst films.[31] As current density is increased, evolution of H^+ by the films is fast, and hence mass transport becomes more pronounced (hence greater spread in $\log(j)$ with rotation rate at higher applied voltage). At high enough $[B_i]$, $\log(j)$ is independent of rotation rate, owing to sufficient buffering capacity, and the overall behavior transitions from mass transport to activation controlled kinetics (indicated by dashed line). The transition occurs at higher $[B_i]$ with higher applied potential (and consequently higher $\log(j)$) because a greater buffering capacity is needed with increased production of H^+. In the region of activation controlled catalysis, the dependence of OER on B_i is furnished from the slope of the solid lines shown in Figure 8. An inverse dependence on $[B_i]$ is observed for CoP_i and CoB_i films. For the latter (Figure 8a), the slopes resides between −0.52 and −0.42, whereas for the CoP_i films (Figure 8b), the slopes are between −0.20 and −0.16. Experiments on CoB_i films were also conducted at pH = 9.2 (Figure S10), and the slopes in the activation controlled region were similar to those collected at pH = 8.6.

■ DISCUSSION

The mechanism of Co-OEC catalyzed water oxidation involves a series of proton-coupled electron transfer (PCET) oxidations leading to an active catalyst. The pathway for OER by CoP_i is shown in Scheme 3.[32] The catalyst is deposited from solution in a Co(III) formal oxidation state (**D**, deposition state).[33] Cobalt K-edge X-ray absorption spectroscopy (XAS)[9] and EPR[34,35] confirm that the catalyst resides in a Co(IV) resting state (**R**). Localized at the edges of the Co-OEC clusters, these Co(IV) centers may be considered to have significant Co(III) oxyl radical character as a direct consequence of the electronic considerations embodied by the "Oxo Wall".[36] Such oxyl radical

Scheme 3. OER Pathway for Co-OEC As Determined from Electochemical Kinetics, EPR, and XAS Studies[a]
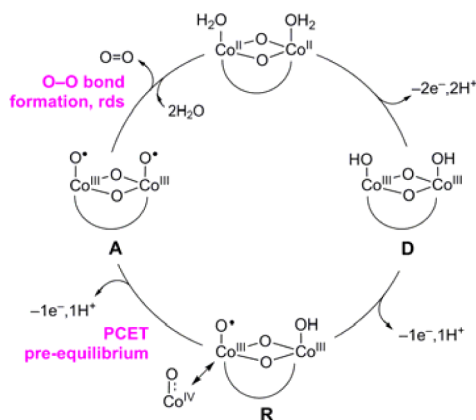

[a]Curved lines denote phosphate, or OH_x terminal or bridging ligands.

character is consistent with increasing evidence for the role of oxygen radicals in O–O bond formation by a PCET mechanism involving water.[18,37−39] A $1e^-/1H^+$ PCET minor equilibrium furnishes the active catalyst (**A**),[12] which drives O–O bond formation and the release of O_2 in a rate-limiting chemical step. The mechanism for O–O bond formation and O_2 generation remains undefined. Two prevailing mechanisms for O–O bond formation rely on the oxyl character of the high-valent metal-oxo: direct intramolecular oxygen coupling (IMOC) of two oxyl radicals leading to a bridging peroxo intermediate (eq 4):

$$(4)$$
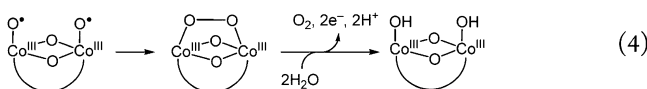
or water hydrogen atom abstraction (WHAA) of an associated water molecule by an oxyl radical, to generate a hydroperoxo intermediate (eq 5):


$$(5)$$
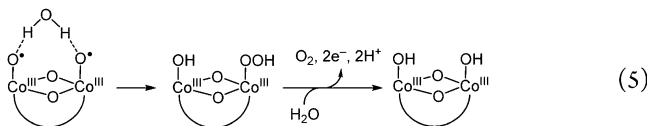
Experimental studies and computational analysis indicate that both mechanisms may be operative for cobalt oxo cubane catalysts. DFT analysis of a Co_4O_4 cubane has suggested that the IMOC mechanism of eq 4 is dominant,[37] and for computations where the WHAA mechanism of eq 5 prevails, it is only slightly favorable (∼5 kcal/mol) as compared to IMOC.[40] Isotopic labeling analysis of a chemically oxidized Co_4O_4 cubane at pH = 12 provides evidence for WHAA, but it is noted that IMOC is kinetically indistinguishable.[41] *In situ* FTIR analysis of crystalline Co_3O_4 nanoparticles (which are known to amorphize to cobaltate clusters at the edges)[13−16] in the presence of a $Ru(bpy)_3^{3+}$ photooxidant at pH = 8 provides evidence toward a WHAA mechanism, by observation of an IR stretching frequency consistent with a hydroperoxo intermediate as shown in eq 5.[18] Conversely, isotopic first turnover analysis of Co/M2P nanoparticles in conjunction with a $Ru(bpy)_3^{3+}$ photooxidant at pH = 7 supports IMOC.[20] The fast exchange that is noted in this work[20] is likely due to the relaxation of Co(III) to Co(II) upon OER,[42] since once the $Ru(bpy)_3^{3+}$ is depleted, a chemical potential does not exist to hold the majority of the cobalt atoms in the catalyst at the

Co(III) oxidation state. In support of this contention, the DEMS data in Figure S2 show that oxidic Co(II) does exchange rapidly; indeed literature values for Co(II) ligand exchange are on the order of 10^6 s^{-1}.[43] This exchange, which complicates the interpretation of the isotope data obtained from a photochemical experiment, may be circumvented in electrochemically driven OER as the applied potential may be poised to maintain a Co(III) oxidation state. Indeed, Figure S1 shows that Co-OEC films composed of ^{18}O evolve significant $^{36}O_2$, even after the films have been equilibrated with natural abundance water for 5 h at room temperature, indicating exchange of terminal OH/OH_2 ligands to be slow. More quantitatively, ^{17}O NMR kinetic analysis of $[\mathbf{1}(OH)(OH_2)]^{3+}$ shows that terminal OH/OH_2 groups exchange slowly with k_{ex} = 4.9 × 10^{-5} s^{-1}. This result is in accordance with known exchange rates of terminal OH/OH_2 mononuclear Co(III) complexes ($k_{ex} \sim 10^{-3}-10^{-6}$ s^{-1}).[29,44] Additionally, the NMR experiment demonstrates that the bridging OH groups lack lability and do not exchange over the span of 28 h.

The detection of $^{36}O_2$ for electrochemically driven water oxidation by ^{18}O-labeled Co-OEC in $H_2^{16}O$ (Figure 1) provides direct evidence that OER proceeds, at least in part, by the IMOC mechanism (eq 4). We note that these isotopic DEMS experiments were only performed at pH = 7, and extrapolation of the results to other pH regimes may not be straightforward. With turnover, the ^{18}O label will be washed out by solvent exchange, accounting for the observation of $^{34}O_2$ and $^{32}O_2$. The appearance of a prompt $^{32}O_2$ signal is a result of partial exchange during equilibration. Based on the rate constant of k_{ex} = 4.9 × 10^{-5} s^{-1} measured from the ^{17}O NMR kinetic analysis, we expect 8% exchange during the 30 min equilibration time of the DEMS experiment. For the 5 h of equilibration experiment, we predict 59% exchange; indeed, we observe a 67% decrease in $^{36}O_2$ signal intensity during this longer equilibration period (Figure S1). A straightforward comparison of theoretical and experimental ratios of O_2 isotopologues is difficult to accurately quantitate because of (i) the low levels of turnover and exchange during the 30 min equilibration period and (ii) an unknown number of film active sites and therefore turnover frequency (TOF). With regard to the latter, in the absence of a measure of TOF, we cannot determine the rate of ^{16}O incorporation with turnover.

The DEMS results cannot distinguish between incorporation of O atoms into the evolved O_2 from either terminal or bridging positions. However, the recent isotopic cubane study by Tilley and co-workers suggests the bridging hydroxos may not be involved in catalysis.[41] The observation that bridging OH ligands are nonexchangeable in the ^{17}O NMR experiment of $[\mathbf{1}(OH)(OH_2)]^{3+}$ also indicates that bridging hydroxos are unreactive during OER. Moreover, we do not believe bridging hydroxos can assume terminal positions via structural rearrangement of the Co-OEC. If there was considerable structural rearrangement of the cobaltate cluster, sufficient ^{18}O label would be continually extruded from the cobaltate cluster interior to produce $^{36}O_2$ after many cycles. This is not the case in Figure 1; $^{36}O_2$ is depleted quickly upon cycling. We emphasize that the DEMS data in Figure 1 do not rule out WHAA as a contributing mechanism to OER. In this case, the $^{34}O_2$ isotopologue would be the primary oxygen product, with $^{32}O_2$ appearing as the label is washed out of the system. The key point with regard to the data in Figure 1 is that the $^{36}O_2$ is unique to the IMOC mechanism.

The DEMs results establish that O−O coupling occurs at the edges of the Co-OEC cobaltate cluster, and thus the OER activity should exhibit a dependence on the nature of the anion. Scheme 1 depicts the basic cobaltate structural unit of Co-OEC with interlayer buffer anions omitted; indeed the actual Co-OEC is capped by P_i or B_i anions that act in the roles of charge balance and proton management.[11,35] The manner in which anions associate and dissociate from the edge site determines whether OER exhibits a buffer dependence. Whereas OER activity of Co-OEC exhibits no dependence on P_i, Figure 8 establishes an inverse dependence on B_i. The more facile binding of B_i to the dicobalt edge site as opposed to P_i is illuminated by the association chemistry of these anions to $[1(OH)_2]^{2+}$. Figure 4 establishes that $B(OH)_3$ is the binding agent in B_i buffer. $B(OH)_3$ can easily and rapidly accommodate coordination of a fourth OH^- to form $B(OH)_4^-$, so association of $B(OH)_3$ to a dicobalt edge site may proceed via nucleophilic attack of $B(OH)_3$ by a bound OH ligand of $[1(OH)_2]^{2+}$. A condensation reaction may then take place between an intermediate borate complex and the adjacent η-OH ligand; a similar mechanism has been proposed for B_i association to FeOOH.[45] In support of this mechanism, we have found activation parameters ($\Delta H^{\ddagger} = 34.5 \pm 0.7$ kJ mol^{-1} and $\Delta S^{\ddagger} = -107 \pm 3$ J mol^{-1} K^{-1}) for this reaction that are consistent with a highly ordered transition state as opposed to breaking of an inert Co(III)−O bond, which would likely lead to a much higher activation enthalpy.[46] The microscopic reverse reaction will also facilitate $B(OH)_3$ dissociation from a dicobalt edge site (eq 6).

$$(6)$$
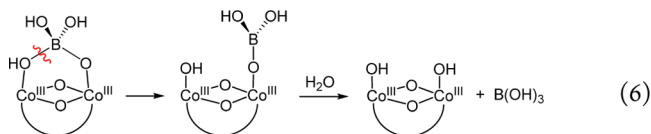
Conversely, direct attack of HPO_4^{2-} by a bound OH ligand of $[1(OH)_2]^{2+}$ is unlikely as phosphate cannot accommodate the coordination of a fifth O atom. Generally, nucleophilic attack of phosphate occurs after Lewis acid activation by a transition-metal center.[47] Thus, the anation of the complex is expected to be very slow due to the rate-limiting dissociative cleavage of the inert Co(III)−O bond.[48] Phosphate dissociation from a dicobalt edge site may proceed by two pathways where HPO_4^{2-} is dissociative (eq 7, left) or is assisted by nucleophilic attack of an external hydroxide (eq 7, right).

$$(7)$$
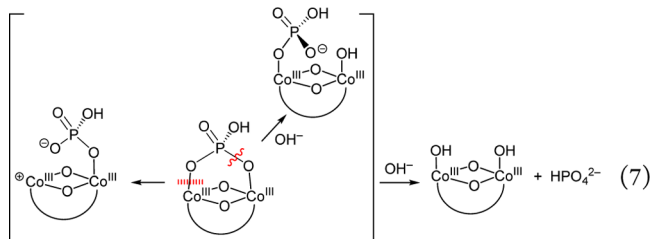
The importance of Co-OEC edge sites in promoting OER has been emphasized in computations.[49] The reactions in eqs 6 and 7 to furnish open coordination sites for O−O bond formation to occur at a dicobalt edge of Co-OEC are manifested in the observed OER activity of the catalysts in B_i and P_i. If anion association to an edge is competitively competent, then OER activity should be inhibited with increasing buffer concentration as fewer edge sites would be available to participate in the PCET activation cycle shown in Scheme 3. At modest to high buffer concentrations ($[P_i] = 40$ mM to 1 M), there is no dependence of $[P_i]$ on water oxidation by Co-OEC.[12] Based on the binding studies of P_i to $[1(OH)_2]^{2+}$, the P_i binding kinetics are likely too slow to establish a pre-equilibrium sufficiently fast to influence the electrochemically driven rate of catalysis, consistent with the zero-order dependence of P_i on the OER current density. Conversely, the B_i binding studies with $[1(OH)_2]^{2+}$ establish that the binding to a dicobalt edge site is sufficiently fast that B_i will have an inhibitory effect on OER, as supported by the dependence of B_i in the activation controlled region of Figure 8. Accordingly, in B_i buffer, optimized OER requires a balance between the need for $B(OH)_4^-$ to accept the protons released from OER and the inhibitory effect of $B(OH)_3$. An additional role of the buffer is control of the morphology of the cobaltate structure.[10] PDF analysis of CoB_i vs CoP_i establishes that the former has a larger domain size of the cobaltate cluster than that in CoP_i. Finally, we propose that the larger domain sizes of CoB_i as compared to CoP_i may be rationalized by considering the disparate exchange kinetics of the capping buffer species on the edge of the growing films.[10] Irreversible binding of P_i to the edge sites may lead to the restriction of particle growth, whereas borate binding does not inhibit growth since borate may be rapidly displaced by incoming Co atoms.

■ CONCLUSION

The OER products of isotopically labeled Co-OEC water splitting catalyst, as determined by differential electrochemical mass spectrometry, indicate that the mechanism of O−O bond formation proceeds, at least in part, by an intramolecular coupling between oxygens atoms bound to the edge sites of the cobaltate catalyst. Binding studies of an edge site dicobalt molecular mimic show that buffer anions of B_i and P_i species mediate the OER activity. Facile changes in boron coordination and the ensuing interaction between B_i and terminal OH ligands explain the inhibitory effect that B_i has on water oxidation activity of Co-OEC, whereas exchange of P_i is too slow to influence the electrochemically driven rate of catalysis. More generally, the cobaltate clusters of Co-OEC lie at the border between extended solid heterogeneous catalysts and polynuclear homogeneous catalysts. We show here that the cobaltate clusters comprising a heterogeneous thin film are amenable to molecular level interrogation and thus exist at molecular/extended solid interface, a domain that has largely been neglected up until now. A dogma of heterogeneous systems is that "edges" matter in promoting catalytic transformations. We provide a rationale for such dogma by showing that OER in cobaltic oxides likely occurs at a dimensionally reduced dicobalt edge site. To this end, the studies reported here begin to unify heterogeneous and homogeneous catalysis at the molecular level.

■ ASSOCIATED CONTENT

ⓈSupporting Information

The Supporting Information is available free of charge on the ACS Publications website at DOI: 10.1021/jacs.6b00762.

Full experimental details, further DEMS data, crystallographic summary, pH titration data, ^{1}H NMR spectra, Job plot, and electrochemical data (PDF)

Crystallographic data (CIF)

Crystallographic data (CIF)

■ AUTHOR INFORMATION

Corresponding Author

*dnocera@fas.harvard.edu

Author Contributions

[†]These authors contributed equally.

Notes

The authors declare no competing financial interest.

■ ACKNOWLEDGMENTS

■ REFERENCES

(1) Lewis, N. S.; Nocera, D. G. *Proc. Natl. Acad. Sci. U. S. A.* **2006**, *103*, 15729.

(2) Lewis, N. S.; Nocera, D. G. *Bridge* **2015**, *46*, 41.

(3) *Electrodes of Conductive Metal Oxides*, Part A; Trasatti, S., Ed.; Elsevier: Amsterdam, 1980.

(4) Surendranath, Y.; Nocera, D. G. *Prog. Inorg. Chem.* **2011**, *57*, 505.

(5) Boggio, R.; Carugati, A.; Trasatti, S. *J. Appl. Electrochem.* **1987**, *17*, 828.

(6) Modestino, M. A.; Walczak, K. A.; Berger, A.; Evans, C. M.; Haussener, S.; Koval, C.; Newman, J. S.; Ager, J. W.; Segalman, R. A. *Energy Environ. Sci.* **2014**, *7*, 297.

(7) Kanan, M. W.; Nocera, D. G. *Science* **2008**, *321*, 1072.

(8) Surendranath, Y.; Dincă, M.; Nocera, D. G. *J. Am. Chem. Soc.* **2009**, *131*, 2615.

(9) Kanan, M. W.; Yano, J.; Surendranath, Y.; Dincă, M.; Yachandra, V. K.; Nocera, D. G. *J. Am. Chem. Soc.* **2010**, *132*, 13692.

(10) Farrow, C. L.; Bediako, D. K.; Surendranath, Y.; Nocera, D. G.; Billinge, S. J. L. *J. Am. Chem. Soc.* **2013**, *135*, 6403.

(11) Du, P.; Kokhan, O.; Chapman, K. W.; Chupas, P. J.; Tiede, D. M. *J. Am. Chem. Soc.* **2012**, *134*, 11096.

(12) Surendranath, Y.; Kanan, M. W.; Nocera, D. G. *J. Am. Chem. Soc.* **2010**, *132*, 16501.

(13) Lee, S. W.; Carlton, C.; Risch, M.; Surendranath, Y.; Chen, S.; Furutsuki, S.; Yamada, A.; Nocera, D. G.; Shao-Horn, Y. *J. Am. Chem. Soc.* **2012**, *134*, 16959.

(14) Friebel, D.; Bajdich, M.; Yeo, B. S.; Louie, M. W.; Miller, D. J.; Sanchez-Casalongue, H.; Mbuga, F.; Weng, T.-C.; Nordlund, D.; Sokaras, D.; Alonso-Mori, R.; Bell, A. T.; Nilsson, A. *Phys. Chem. Chem. Phys.* **2013**, *15*, 17460.

(15) Bergmann, A.; Martinez-Moreno, E.; Teschner, D.; Chernev, P.; Gliech, M.; Ferreira de Araujo, J.; Reier, T.; Dau, H.; Strasser, P. *Nat. Commun.* **2015**, *6*, 8625.

(16) Gonzalez-Flores, D.; Sanchez, I.; Zaharieva, I.; Klingan, K.; Heidkamp, J.; Chernev, P.; Menezes, P. W.; Driess, M.; Dau, H.; Montero, M. L. *Angew. Chem., Int. Ed.* **2015**, *54*, 2472.

(17) Zhang, M.; Frei, H. *Catal. Lett.* **2015**, *145*, 420.

(18) Zhang, M.; de Respinis, M.; Frei, H. *Nat. Chem.* **2014**, *6*, 362.

(19) Plaisance, C. P.; van Santen, R. A. *J. Am. Chem. Soc.* **2015**, *137*, 14660.

(20) Koroidov, S.; Anderlund, M. F.; Styring, S.; Thapper, A.; Messinger, J. *Energy Environ. Sci.* **2015**, *8*, 2492.

(21) Wang, H.; Rus, E.; Sakuraba, T.; Kikuchi, J.; Kiya, Y.; Abruna, H. D. *Anal. Chem.* **2014**, *86*, 6197.

(22) Peng, Z.; Freunberger, S. A.; Chen, Y.; Bruce, P. G. *Science* **2012**, *337*, 563.

(23) Jusys, Z.; Kaiser, J.; Behm, R. J. *Langmuir* **2003**, *19*, 6759.

(24) Baltruschat, H. *J. Am. Soc. Mass Spectrom.* **2004**, *15*, 1693.

(25) Wang, H.; Abruña, H. In *Electrocatalysis of Direct Alcohol Fuel Cells: Quantitative DEMS Studies Fuel Cells and Hydrogen Storage*; Bocarsly, A., Mingos, D. M. P., Eds.; Springer: Berlin, 2011; Vol. *141*, pp 33−83.

(26) Davenport, T. C.; Tilley, T. D. *Angew. Chem., Int. Ed.* **2011**, *50*, 12205.

(27) Davenport, T. C.; Tilley, T. D. *Dalton Trans.* **2015**, *44*, 12244.

(28) Davenport, T. C.; Ahn, H. S.; Ziegler, M. S.; Tilley, T. D. *Chem. Commun.* **2014**, *50*, 6326.

(29) Aygen, S.; Hanssum, H.; van Eldick, R. *Inorg. Chem.* **1985**, *24*, 2853.

(30) Müller, B. *ChemEQL*, ver. 3.1; Limnological Research Center EAWAG/ETH: Kastanienbaum, Switzerland, 2009.

(31) Bediako, D. K.; Costentin, C.; Jones, E. C.; Nocera, D. G.; Savéant, J.-M. *J. Am. Chem. Soc.* **2013**, *135*, 10492.

(32) Bediako, D. K.; Ullman, A. M.; Nocera, D. G. *Top. Curr. Chem.* **2015**, *371*, 173.

(33) Surendranath, Y.; Lutterman, D. A.; Liu, Y.; Nocera, D. G. *J. Am. Chem. Soc.* **2012**, *134*, 6326.

(34) McAlpin, J. G.; Surendranath, Y.; Dincă, M.; Stich, T. A.; Stoian, S. A.; Casey, W. H.; Nocera, D. G.; Britt, R. D. *J. Am. Chem. Soc.* **2010**, *132*, 6882.

(35) Gerken, J. B.; McAlpin, J. G.; Chen, J. Y. C.; Rigsby, M. L.; Casey, W. H.; Britt, R. D.; Stahl, S. S. *J. Am. Chem. Soc.* **2011**, *133*, 14431.

(36) Winkler, J. R.; Gray, H. B. In *Structure and Bonding (Berlin)*; Mingos, D. M. P., Day, P., Dahl, J. P., Eds.; Springer: Berlin Heidelberg, 2012; Vol. *142*; p 17.

(37) Wang, L.-P.; Troy, V. V. *J. Phys. Chem. Lett.* **2011**, *2*, 2200.

(38) Jiang, Y.; Li, F.; Zhang, B.; Li, X.; Wang, X.; Huang, F.; Sun, L. *Angew. Chem., Int. Ed.* **2013**, *52*, 3398.

(39) Yang, X.-H.; Baik, M. *J. Am. Chem. Soc.* **2006**, *128*, 7476.

(40) Li, X.; Siegbahn, P. E M. *J. Am. Chem. Soc.* **2013**, *135*, 13804.

(41) Nguyen, A. I.; Ziegler, M. S.; Ona-Burgos, P.; Sturzbecher-Hoehne, M.; Kim, W.; Bellone, D. E.; Tilley, T. D. *J. Am. Chem. Soc.* **2015**, *137*, 12865.

(42) Lutterman, D. A.; Surendranath, Y.; Nocera, D. G. *J. Am. Chem. Soc.* **2009**, *131*, 3838.

(43) Ohlin, C. A.; Harley, s. J.; McAlpin, J. G.; Hocking, R. K.; Mercado, B. Q.; Johnson, R. L.; Villa, E. M.; Fidler, M. K.; Olmstead, M. M.; Spiccia, L.; Britt, R. D.; Casey, W. H. *Chem. - Eur. J.* **2011**, *17*, 4408.

(44) Bradley, S. M.; Doine, H.; Krouse, H. R.; Sisley, M. J.; Swaddle, T. W. *Aust. J. Chem.* **1988**, *41*, 1323.

(45) Peak, D.; Luther, G. W., III; Sparks, D. L. *Geochim. Cosmochim. Acta* **2003**, *67*, 2551.

(46) Swaddle, T. W. *Coord. Chem. Rev.* **1974**, *14*, 217.

(47) Williams, N. H.; Takasaki, B.; Wall, M.; Chin, J. *Acc. Chem. Res.* **1999**, *32*, 485.

(48) Chin, J.; Banaszczyk, M.; Jubian, V.; Zou, X. *J. Am. Chem. Soc.* **1989**, *111*, 186.

(49) Mattioli, G.; Giannozzi, P.; Bonapasta, A. A.; Guidoni, L. *J. Am. Chem. Soc.* **2013**, *135*, 15353.